

Proton- CAT: a Novel Enhanced Proton Treatment Approach

Zhao Sun¹, Zhencen He^{2,1}, Junxiang Wu^{1,3}, Liyuan Deng¹, Zhuohang He¹, Ziqi Chen¹, Junkang Jiang¹, Hang Zhu¹, Shuyu Zhang² and Zhimin Hu^{1,*}

¹Key Laboratory of Radiation Physics and Technology of Ministry of Education, Institute of Nuclear Science and Technology, Sichuan University, Chengdu 610064, China

²West China School of Basic Medical Sciences and Forensic Medicine, Sichuan University, Chengdu 610041, China

³Radiation Oncology Department Sichuan Cancer Hospital and Institute, Affiliated Cancer Hospital of University of Electronic Science and Technology of China, Chengdu 610041, China,

Abstract

Proton therapy is deemed the cornerstone of cancer treatment and is regarded as one of the fastest-developing therapeutic modalities. The development of new methods to enhance the biological effectiveness of proton therapy (PT) is a focal point in the field of radiation oncology research. This work introduced a novel nitrogen-targeted proton-carbon-alpha therapy approach, Proton-CAT, which involves the generation of carbon-12 and alpha particles through the interaction of protons with nitrogen-15. This therapy is based on the reaction of proton capture by the ¹⁵N isotope. Here, we validated the effectiveness of Proton-CAT using Monte Carlo simulations and compared it with proton boron capture therapy (PBCT). The energy deposition distribution was studied in both single Bragg peak and the spread-out Bragg peak (SOBP) regions. In the SOBP region, the generated secondary particles were analyzed. Furthermore, the contribution of α -particles to the dose was calculated based on the different target materials. The obtained results expand the avenues for binary radiotherapy and are expected to contribute to the future development of proton therapy.

Keywords: Proton therapy, Nitrogen-Targeted Proton-Carbon-Alpha Therapy (Proton-CAT), Monte Carlo method, Spread-out Bragg peak, Dose enhancement

Introduction

In this century, cancer is poised to emerge as the predominant cause of premature mortality worldwide, presenting the most formidable obstacle to further extending life expectancy[1]. Presently, the majority of clinical radiotherapy employs photon beams with energy ranging from 4 to 18 megavolts (MV). However, given the physical characteristics of photons, substantial doses of unnecessary radiation are still received by the normal tissues surrounding the target volume.

For many years in parallel, proton therapy (PT) has been developing tempestuously based on

* Corresponding author
E-mail: huzhimin@scu.edu.cn

the physical properties of the Bragg curve[2–4]. These properties can provide extremely high dose gradients near organs at risk, thereby confining the high-dose area within the tumor volume. Within the Bragg peak, energy is deposited in a clustered rather than sparse form of ionization events. This results in more complex DNA damage that is harder or even impossible to repair through enzymatic DNA repair mechanisms, leading to enhanced biological effects. While this may be advantageous in tumors, it can be detrimental to normal tissues near the tumor[5]. Achieving local tumor control may necessitate delivering the full or near-full dose, emphasizing the need for optimizing the dose-effect relationship between tumors and surrounding normal tissues. Therefore, despite the evident physical advantages of PT, addressing the challenge of improving the dose effectiveness in tumors relative to nearby normal tissues is fundamental to enhancing the efficiency of PT.

To solve the aforementioned challenge, binary radiotherapy (BRT) techniques are gradually finding application in clinical settings as an innovative approach[6,7]. During treatment, a non-toxic and side-effect-free targeted specific agents are initially enriched in the tumor volume. These specific agents exhibit strong affinity for tumor cells, rapidly accumulating within them while having minimal distribution in normal tissues. Subsequently, neutrons and protons are applied to the region enriched with the targeted agents. The radiation induces nuclear reactions with the targeted drug, generating particles with high linear energy transfer (LET) which can selectively damage tumor cells without adversely affecting normal tissues [7]. With the development of PT, proton boron capture therapy (PBCT) method was proposed by Yoon, et al [8]. Its purpose is to increase the cumulative dose delivered to the target area without escalating the dose on normal tissues. This is achieved by capitalizing α particles after the proton boron fusion reaction (PBFR: $p+^{11}\text{B}\rightarrow 3\alpha$). PBCT utilize targeted agents containing boron isotopes, primarily boronophenylalanine ($\text{C}_9\text{H}_{12}\text{BNO}_4$, BPA) and sodium mercaptoundecahydrododecaborate ($\text{Na}_2\text{B}_{12}\text{H}_{11}\text{SH}$, BSH) [9]. It produces α particles with energies in the range of several MeV, which have a limited penetration range and can induce cellular damage in the vicinity of the reaction site. However, there are many controversies with this solution in practice [10–14]. Cirrone et al. conducted in vitro studies using the PBFR reaction with a clinical proton beam[10]. Their findings suggest that the effectiveness of proton therapy was enhanced when an appropriate concentration of BSH was added to prostatic tumor cells. The results indicate a significant decrease in cell survival rates with the presence of boron and PBCT was only effective at depths where low-energy protons are present. Additionally,

extensive use of Monte Carlo simulations in PBCT studies for PT indicated significant dose enhancement in regions where boron absorption coincides with the Bragg peak [11,12]. However, some researchers put forward the opposite opinion [13,14]. They argue that using BSH/BPA only leads to a marginal increase of boron uptake in tumor tissues compared to healthy tissues. This modest boron concentration was considered impossible to result in a substantial increase in alpha particle dose, thus diminishing the enhancement of biological effectiveness. On the other hand, the maximum reaction cross-section for PBFR occurs at 0.6~1.0 MeV, which is not compatible with the residual energy of protons in the Bragg peak region [15,16]. Despite some optimistic experimental results, the limitations of PBCT are too significant due to the concentration of boron compounds. Therefore, expanding the utilization of proton-targeted therapy is pressing for promoting BRT technology, as current reliance on boron-containing drugs alone proves insufficient.

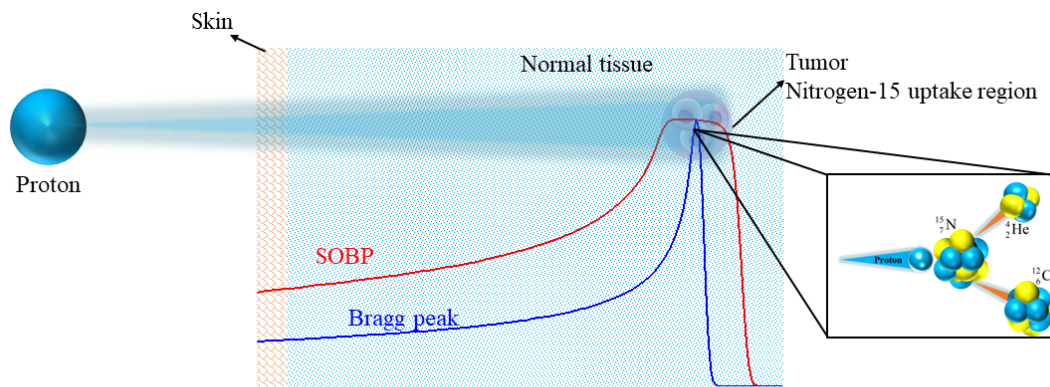


Fig. 1 Conceptual diagram of Proton-CAT.

Inspired by PBCT and in order to meet the development challenges of proton therapy, we present a novel BRT technique called Nitrogen Targeting Proton-Carbon-Alpha Therapy (Proton-CAT). This innovative approach is based on the proton and nitrogen (^{15}N) fusion reaction (PNFR), which initially proposed by A. Schardt [17]:

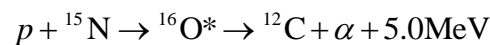


Fig. 1 shows the schematic diagram of Proton-CAT. This nuclear reaction exhibits a relatively high cross-section when the proton energy ranges from 4 to 11 MeV, releasing a substantial amount of energy. Simultaneously, the interaction between protons and ^{15}N leads to the fragmentation of the excited oxygen atom (^{16}O) into carbon (^{12}C) and α particles. The generated ^{12}C particles not only

have the same physical advantages as protons in Bragg peak, but also belong to dense ionized particles, which belong to high LET rays in the whole energy range, and their LET values will change with the depth. α particles possess high radiation energy, allowing for precise tumor cell destruction without affecting surrounding normal tissues. Therefore, biological damage and RBE are significantly elevated compared to PT. [18,19]. In Proton-CAT, ^{15}N -labeled glutamine ($\text{C}_5\text{H}_{10}\text{N}_2\text{O}_3$) can serve as a targeted drug in Proton-CAT. According to research, compared with normal cells, tumors such as stomach, colorectal and breast cancer have higher intake of glutamine [20]. In addition, ammonium citrate ($\text{C}_6\text{H}_{17}\text{N}_3\text{O}_7$), uracil ($\text{C}_4\text{H}_4\text{N}_2\text{O}_2$), tryptophan ($\text{C}_{11}\text{H}_{12}\text{N}_2\text{O}_2$), glycine ($\text{C}_2\text{H}_5\text{NO}_2$), etc., which is nitrogen-containing drugs with good uptake in tumor cells can also serve as targeted drugs, representing one of the advantages of our approach. These meet the criteria of high tumor uptake, low normal tissue absorption, low toxicity, and rapid clearance after treatment[21]. By combining physical and biochemical targeting, proton therapy has the potential to effectively target malignant cells while minimizing excessive radiation to surrounding tissues. The secondary particles generated can also contribute to killing cancer cells within the cellular range.

In this study, we assessed the energy deposition of protons in tumors and validated the theoretical efficacy of Proton-CAT through Monte Carlo simulations. We further investigated the potential benefits of enhancing ^{15}N concentration in Proton-CAT for proton therapy and compared it with PBCT. Additionally, the secondary particles produced by both Proton-CAT and PBCT was calculated, aiming to quantify the contribution of each nuclear reaction to secondary particles and assess whether they could achieve a synergistic effect for dose enhancement. The purpose of this work was to create a new potential PT technology for cancer patients and significantly increase the RBE of PT.

2. Simulated Calculation and Method

2.1 Geant 4 toolkit and Physical List

The Geant 4 toolkit is an open-source Monte Carlo simulation program widely used in medical physics[22]. In the current work, the physical list employed for all simulations is G4HadronPhysics QGSP_BIC_AllHP. It employs the binary cascade de-excitation model, electromagnetic physics option 4 as the standard, and a precision data-driven model for low-energy protons, neutrons,

deuterium, tritium, ^3He , and alpha particles. An assessment of both the binary cascade and standard electromagnetic physics option4 has been conducted to ensure optimal agreement between simulated results and measurements in proton therapy[23]. In addition, it is created with the High-Precision Charged Particle physics model, which is suitable for energy below 200 MeV. The range threshold for all secondary particles production was set to 0.1 mm, below which the projectile trajectory is terminated and all remaining kinetic energy is deposited locally.

2.2 The method of generating Spread-Out Bragg Peak using pristine Bragg curves

As we all know, single-energy proton beam is not suitable for cancer treatment because of the narrow Bragg peak in the longitudinal direction. Therefore, to enhance the precise treatment of tumors with varying shapes and depths, the Spread-Out Bragg Peak (SOBP) allows for the creation of a continuous flat dose distribution within a specific depth in the target volume[24,25]. The SOBP is formed by multiple Bragg curves with various implant energies are superimposed using appropriate beam weights. In this study, two SOBPs with different widths and depths were created by using the modified method in Ref. [25]. In addition, the residual energy $E(r_k)$ at Bragg peak of per pristine curves r_k (cm) can be determined by the Geiger's rule for the proton range (R_0) in a material [26]:

$$E(r_k) = \left(\frac{R_0 - r_k}{\alpha} \right)^{1/p}$$

In the equation, the material-dependent parameters α and p are assigned the numerical values of 2.253×10^{-3} (cm/MeV p) and 1.77461 for water, respectively. Detailed weights of two SOBPs are summarized in Table 1. As shown in Fig. 2, two SOBPs are created in Geant 4, and both exhibit an extended plateau region. SOBP5 has a depth of 5 cm and the widths is 8 mm, while SOBP15 has a depth of 15 cm and the widths is 22.5 mm.

Table 1 The parameters used to create SOBP5 and SOBP15, where k is the index of single-energy Bragg peaks contributing to the formation of SOBP, r_k is the position of Bragg peak with corresponding energy, and w_k is the weight of corresponding energy.

SOBP5	SOBP15
-------	--------

k	Energy (MeV)	r_k (cm)	w_k (%)	E (r_k) (MeV)	Energy (MeV)	r_k (cm)	w_k (%)	E (r_k) (MeV)
1	71.38	4.20	2.15	12.05	133.67	12.75	2.01	23.37
2	72.14	4.28	4.52	12.17	135.00	12.98	4.26	23.52
3	72.90	4.36	4.85	12.31	136.32	13.20	4.62	23.88
4	73.66	4.40	5.26	13.83	137.62	13.43	5.05	23.98
5	74.40	4.52	5.76	12.58	138.92	13.65	5.58	24.34
6	75.14	4.60	6.41	12.71	140.21	13.88	6.28	24.47
7	75.88	4.68	7.3	12.86	141.49	14.10	7.22	24.82
8	76.61	4.76	8.64	12.99	142.76	14.33	8.63	24.94
9	77.33	4.84	10.96	13.10	144.03	14.55	11.06	25.31
10	78.05	4.92	16.78	13.23	145.28	14.78	17.10	25.42
11	78.77	5.00	27.37	13.38	146.53	15.00	28.19	25.77

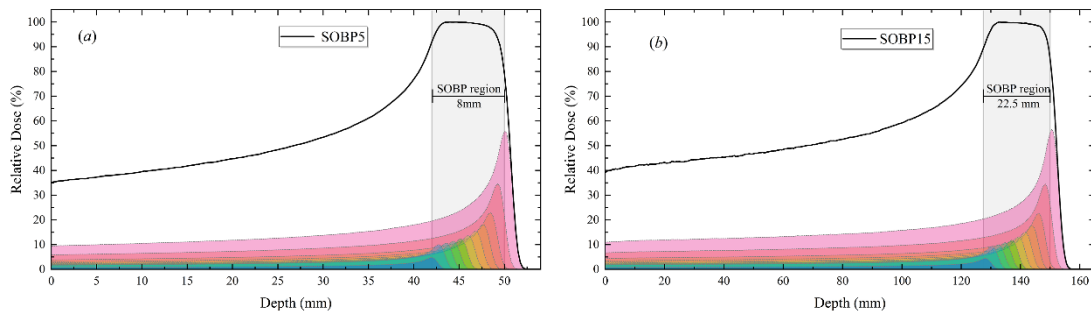


Fig. 2 The expected (a) SOBP5 and (b) SOBP15 curves along with all weighted pristine depth-dose curves.

2.3 Model parameters and assumptions of simulation

In Geant 4, the simulated geometric principle of target is shown in Fig. 3. The target is made up of water and tumor phantom. The material of tumor region is defined as a mixture and be grouped under three heads, including ^{11}B or ^{15}N with various concentrations as shown in Table 2. Both the phantom and tumor are defined as cubes with a side length of 10 cm. A proton beam with assigned energy is directed from the front of the water, covering the entire target volume. Therefore, as shown in Table 3, the thicknesses (x, y) of the water and the tumor phantom depend the incident proton

energy to ensure the entire Bragg Peak covers the tumor region. The proton energies employed monoenergetic (75, 140 MeV) and multiple energies with calculated weights for each energy in Table 1.

In our work, for each simulation run, 10^9 protons are transported through the target volume, encompassing the water and the tumor phantom region with various materials in Table 2. For the four tumor phantom (Pure water, 90% Water + 10% ^{11}B , 90% Water + 10% ^{15}N and 70% Water + 30% ^{15}N), the parameters specified in Table 3 are selected. To compare concentration differences, the composition of 70% water + 30% ^{15}N was employed.

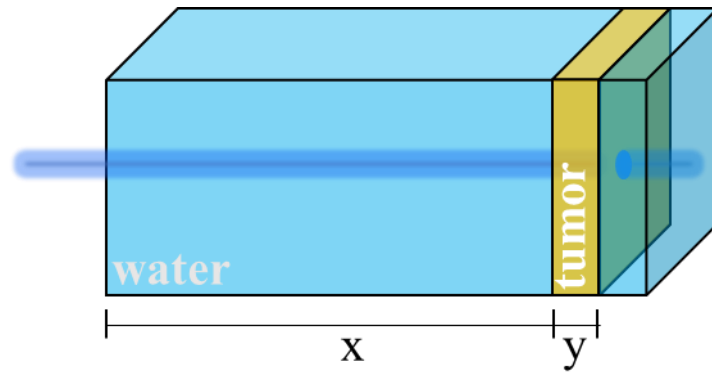


Fig. 3 The principle of target.

Table 2 Compositions, mass density and elemental composition of the three-group tumor phantom.

Groups	Mass density (g/cm ³)	H	O	¹¹ B	¹⁵ N
90% Water+10% ¹¹ B	1.226	60	30	10	0
90% Water+10% ¹⁵ N	1.139	60	30	0	10
70% Water+30% ¹⁵ N	1.538	46.7	23.3	0	30

Table 3 The thicknesses of water (x) and tumor (y) phantom.

Energy	x (cm)	y (cm)
75 MeV	4.10	0.50
140 MeV	13.50	1.00
SOBP5	4.20	0.80
SOBP15	12.75	2.25

3. Results and discussion

3.1 Depth dose calculation(Single Bragg peak and SOBP)

Fig. 4 shows the relative energy deposited (RED) in target volume under mono-energy proton implanted. The RED in the pure water was used as the reference. The RED increases with depth and reaches a Bragg peak near the maximum range. Compared to pure water, the doping of ^{11}B and ^{15}N can enhance the energy deposition in the tumor volume and cause a forward shift of the Bragg peak. At the same doping concentration, the energy deposition is higher for ^{11}B compared to ^{15}N . Due to protons release their last few MeV of kinetic energy upon reaching tumor region (the energy range with the largest nuclear reaction cross section), it leads to an increase in selectivity of the PBCT and Proton-CAT [14]. The nuclear reaction with ^{11}B and ^{15}N is responsible for the large energy delivery. These deliveries become more considerable as the concentration of ^{15}N increases to 30%.

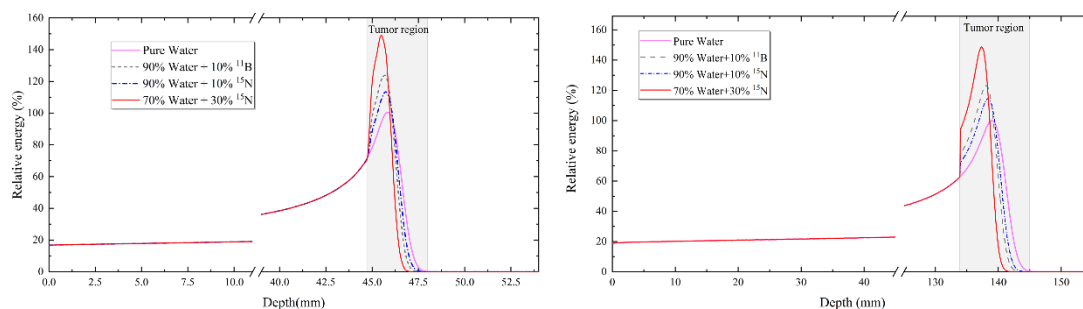


Fig. 4 The RED curves of different tumor. The monoenergetic proton energies were (a) 75 and (b) 145 MeV.

In addition, from the Fig. 4 (b), it can be observed that the accumulation of range straggling tends to broaden the peak with increasing depth. Nonetheless, the monoenergetic proton beam has a finite range and the deposited energy is un-homogeneous in tumor volume. Moreover, this finite range becomes more constrained with variations in the doping concentration within the tumor region. Therefore, we obtained the RED curve with SOBP5 and SOBP15, as shown in Fig. 5. After setting SOBP5 and SOBP15, the deposited energy by SOBP exhibits a significant increase in the tumor region, similar to the case of monoenergetic protons. However, the difference is that the maximum energy deposition can cover the whole tumor region. Moreover, in the SOBP region, due to the change of concentration and density, adding targeted elements will also narrow the maximum energy

range, which can be reduced by 30%. This is crucial and represents a potential disadvantage that must be overcome in practical clinical treatments to optimize the safety and efficacy of the approach.

Whether it is monoenergetic or an SOBP proton energy, the energy deposition by PBCT is higher than that of Proton-CAT under the same targeted element concentration. This is evident, because the energy released from the reaction between protons and ^{11}B (8.6 MeV) is more than with ^{15}N (5.0 MeV) [17,27]. However, as evident from both Figs. 4 and 5, threefold increase in the concentration of ^{15}N in the tumor region significantly leads to an increased frequency of nuclear reactions and then the energy deposition of protons in the tumor region. Therefore, to prevent the protons from depositing their energy beyond the target, both appropriate modulation of the SOBP width and consideration of increasing the concentration of ^{15}N can be considered.

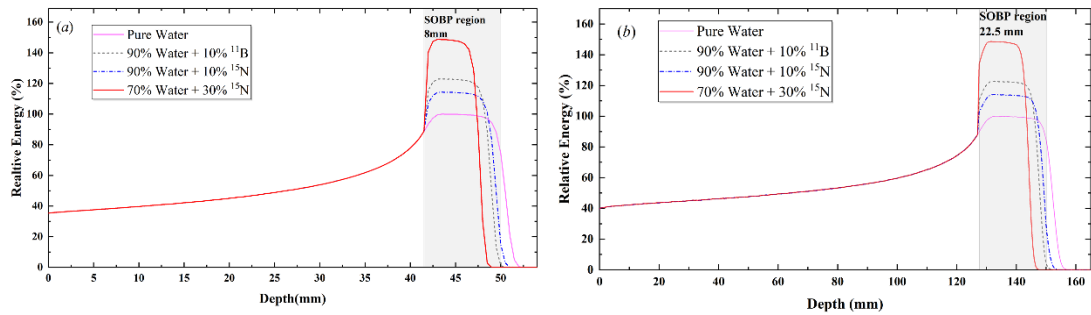


Fig. 5 The RED curves of different tumor. The proton energies were (a) SOBP5 and (b) SOBP15.

3.2 Production of secondary particles

This study exploits the nuclear reactions between protons and targeting elements to enhance the dose through the production of heavy secondary particles. In the SOBP region, the energy spectra and yields of emitted secondary particles (^{12}C and α) produced by nuclear reactions of PBCT and Proton-CAT were statistically analyzed. Figs. 6 and 7 shows the energy spectra of ^{12}C and α particles emitted after the reactions between protons and dopant elements (^{11}B and ^{15}N) in the SOBP5 and SOBP15 region. As observed in Fig. 6(a), the contribution of ^{12}C was primarily due to the reactions involved in Proton-CAT, because it will not occur in $p+^{11}\text{B}$ reactions. The generated ^{12}C was mainly distributed in the 2~4 MeV, with the highest peak occurring at 5.9 MeV. Compared to ^{12}C , the energy spectrum distribution of α particles was more uniform. The nuclear reaction processes of PBCT and Proton-CAT both generate α particles, with energy primarily distributed in 2~10 MeV.

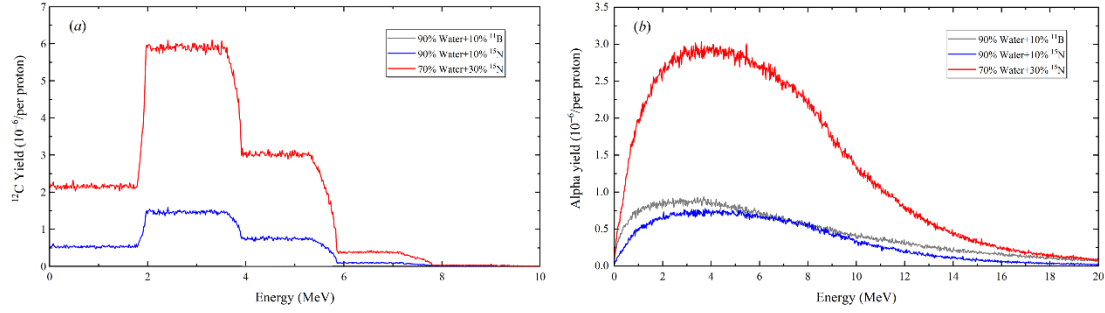


Fig. 6 In SOBP5 region, the energy spectra of the emitted (a) ^{12}C and (b) α particle induced by the reaction between the proton and doping elements.

Moreover, it can be seen from the energy spectrum of SOBP15 region in Fig. 7 that expanding the depth and width of SOBP can increase the yield of ^{12}C . Especially for α , its yield doubles compared to SOBP5 in both PBCT and Proton-CAT. These changes can be quantified through the statistical counting of secondary particles generated after the implantation of 10^9 protons, as shown in Fig. 8.

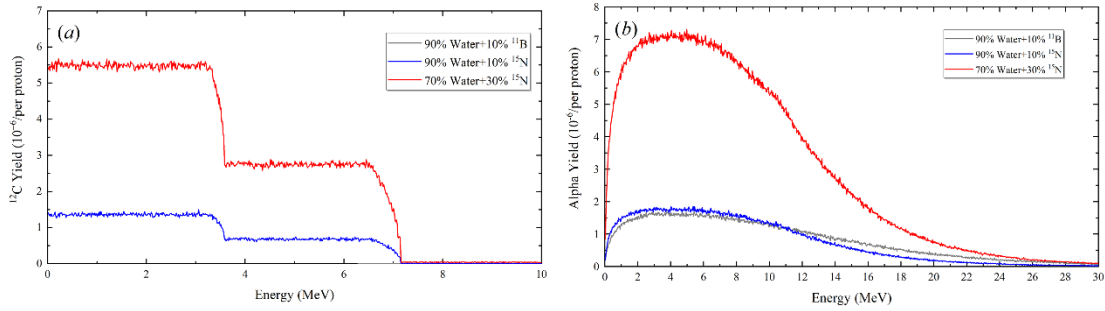


Fig. 7 In SOBP15 region, the energy spectra of the emitted (a) ^{12}C and (b) α particle induced by the reaction between the proton and doping elements.

It can be clearly seen that in the SOBP5 region from Fig. 5 (a), the number of ^{12}C generated by Proton-CAT was equal to α , which is in accordance with the nuclear reaction equation ($\text{p}+^{15}\text{N}\rightarrow^{12}\text{C}+\alpha$). However, an important finding was that at the same 10% concentration, the α number in the SOBP region for PBCT was only slightly higher than that of Proton-CAT. Base on theoretical and experimental studies on PBFR indicated that the highest cross section of PBFR occurs at the proton with energy of 0.6~1.0 MeV [15,16]. High-energy protons in the SOBP region (tumor) retain relatively high residual energy, while cross-section of PBFR was lesser than PNFR in this energy range. On the contrary, Proton-CAT can demonstrate its advantage in the SOBP region, producing α equivalent to PBCT and additional ^{12}C . These become more evident in the SOBP15 region, as shown in Fig. 5(b). In addition, not only is the number of ^{12}C particles no longer equal to

α in this region, but also to clarify from which energy range the increased ^{12}C and α come compared to the SOBP5 region. We conducted segmented statistics of the spectra in Figs. 6 and 7, the results are shown in Fig. 9.

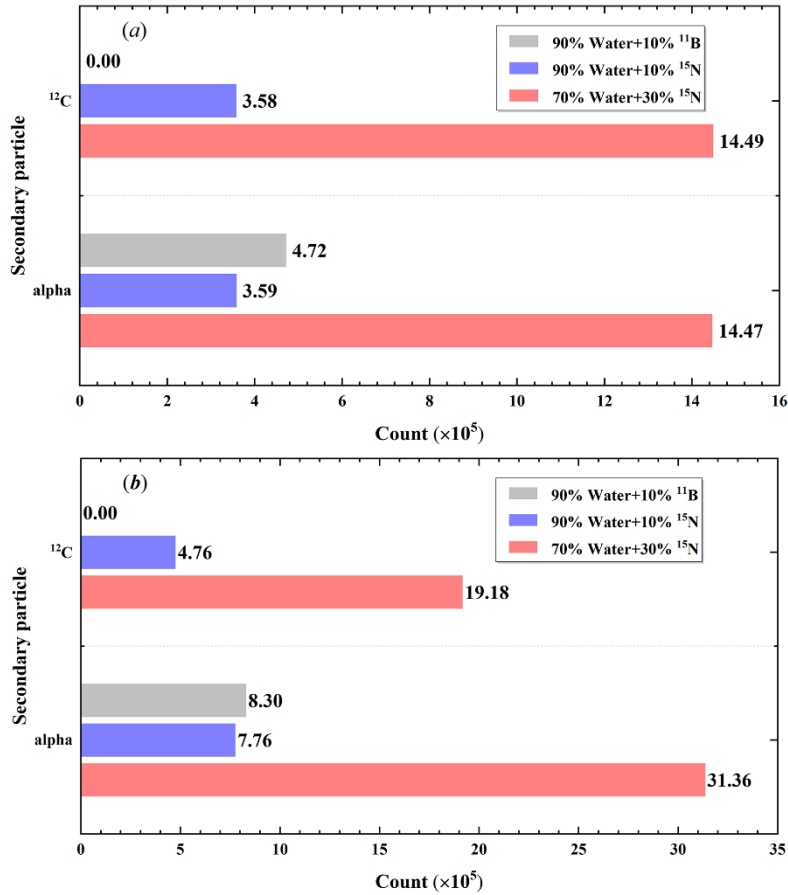


Fig. 8 After the incidence of 10^9 protons, the statistical count of ^{12}C and α particles generated through the nuclear reaction processes of PBCT and Proton-CAT, (a) SOBP5 and (b) SOBP15.

From the segmented statistical results of carbon in Fig. 9(a), compared to the SOBP5 region, the ^{12}C will increase manyfold with energy in the range of 0~2 MeV in the SOBP15 region. The production of ^{12}C in the range of 4~7 MeV has also increased. These contribute significantly to the gain of ^{12}C in Fig. 8 (a) and (b). There are some important differences between ^{12}C and α . In the SOBP15 region, the number of α across increased significantly in all energy regions, with the increase predominantly among the high-energy region as shown in Fig. 9 (b). In Proton-CAT, whether at 10% or 30% concentration of ^{15}N , the high-energy α particle count in the SOBP15 region prominently exceeded threefold. A further novel finding is that plentiful α with energy $> 8\text{MeV}$ in PBCT are found in a wider SOBP region. These variations are attributed to the larger residual energy of protons in the SOBP15 region. As shown in Table 1, protons deposit the remaining energy in the

SOBP region. The residual energy of protons in the SOBP15 region was sufficient to activate the $^{11}\text{B}(p, \alpha)^8\text{Be}$ and $^{15}\text{N}(p, \alpha)^8\text{Be}$ channels, leading to the generation of high-energy α particles [28]. Correspondingly, the residual energy was lower in the narrower and shallower SOBP5 region, leading to a reduced production of high-energy α particles, especially in PBCT. Therefore, the production of α particles by protons in the SOBP15 region is higher than that of ^{12}C , as shown in Fig. 8(b).

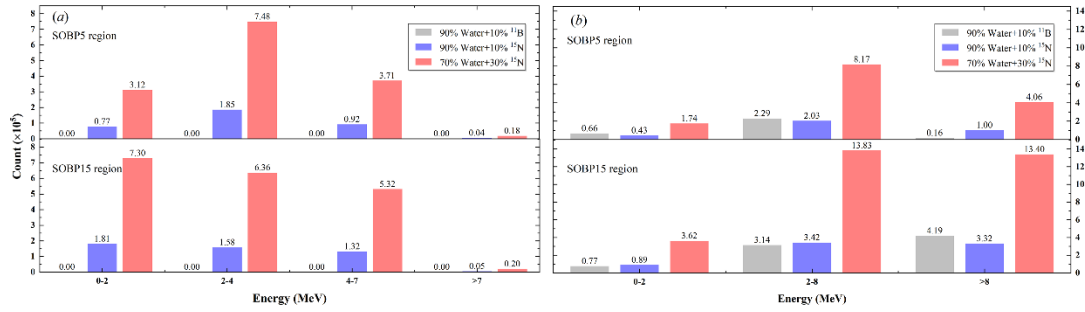


Fig. 9 After the incidence of 10^9 protons, segmented statistical results of the energy of secondary particles generated by PBFR/PNFR in the SOBP5 and SOBP15 regions.

3.3 Analysis of therapeutic effectiveness

From the results in Sections 3.1 and 3.2, we can see that under the clinical SOBP conditions, both Proton-CAT and PBCT lead to an increase in deposited energy in the tumor region. In PT, the therapeutic effect was caused by both primary and secondary particles. Through the analysis mentioned above, both Proton-CAT and PBCT generate a large number of secondary particles. They contribute to the total absorbed dose. Moreover, they have high LET values, leading to an increase in the RBE of the proton beam. Therefore, based on the results for SOBP5 and SOBP15, we calculated the dose enhancement due to secondary α particles in the SOBP region.

Table 4 The absorbed doses (mGy) in the only tumor region for α particle.

Tumor material	Absorbed dose (mGy)			
	75 MeV	140 MeV	SOBP5	SOBP15
Pure water	2.7014×10^{-2}	7.0447×10^{-2}	0.6626	0.1322
90% water +10% ^{11}B	4.5931×10^{-2}	7.3652×10^{-2}	0.6978	0.1266
90% water +10% ^{15}N	4.2539×10^{-2}	7.7717×10^{-2}	0.7300	0.1264

70% water +30% ^{15}N	6.1063×10^{-2}	8.4374×10^{-2}	0.7884	0.1146
--------------------------------	-------------------------	-------------------------	--------	--------

Table 4 only provides the dose enhancement of α particles generated by Proton-CAT and PBCT in the Bragg peak and SOBP regions. It can be observed that when 75 MeV protons were implant on the tumor target with widths of 0.5 cm, the absorbed dose of α particles produced by and Proton-CAT increases significantly compared to pure water . Analogously, when increasing the proton beam energy (140 MeV) and the width of the tumor region (1.0 cm), the absorbed dose enhancement from PBCT was reduced. However, PNFR has the overflowing expected absorbed dose with the increase of ^{15}N concentration, being the dose related to this reaction orders of higher than the dose delivered by the primary proton beam. On the other hand, the absorbed dose generated by Proton-CAT exceeds that of the primary proton beam in the SOBP5 region, especially when compared to PBCT. As shown in Fig. 9, Proton-CAT can produce enormous ^{12}C with 0-7 MeV, further enhancing the dose in the tumor region. Different from the SOBP5 region, the dose enhancement effect was further weakened in the SOBP15 region that similar to the case with 140 MeV protons, especially for PBCT. The reason for these phenomena was that high-energy protons retain large energy in the tumor area. PBFR exhibits a lower reaction cross-section. Furthermore the $^{16}\text{O}(p, \alpha)^{13}\text{N}$ nuclear reaction has a relatively low threshold (5.66 MeV), leading to the generation of more α particles in water[29]. The doping elements ^{11}B and ^{15}N absorb some protons, thereby reducing the absorbed dose.

Therefore, both PBCT and Proton-CAT was not satisfactory with monoenergetic low-energy proton beams. Under clinically relevant SOBP condition, Proton-CAT achieves a prospective dose enhancement in the SOBP5 region. However, as shown in Fig. 9, although it generates a substantial amount of ^{12}C and α particles in the SOBP15 region, a significant portion of these α particles is high-energy. With an increase in ^{15}N concentration, these high-energy α particles become disadvantageous in Proton-CAT. In conclusion, utilizing Proton-CAT therapy is a favorable choice in superficial treatment due to its ability to enhance dose efficiency while covering the tumor.

Conclusion

In the present work, a novel enhanced proton treatment approach Proton-CAT based on the nuclear reaction between protons and ^{15}N was proposed. Monte Carlo simulations were employed

to evaluate the performance of Proton-CAT in proton therapy and compared it with PBCT. In addition, varying concentrations of ^{15}N were set to contrast the impact of concentration enhancement on energy deposition and the generation of secondary particles. Comparison was also made between a single Bragg peak and SOBP in terms of energy deposition, generation of secondary particles, and other performance aspects. To quantitatively assess the efficacy of α -particle dose deposition in various scenarios, the average dose of secondary α -particles in the tumor region was determined. These results indicated that Proton-CAT demonstrates a dose enhancement advantage in low-energy proton therapy. However, for higher incoming proton energies, normal tissues also generate α -particles, and the dose advantage of ^{12}C and α produced by Proton-CAT was not significant. It must be emphasized that, despite our results confirming the fundamental effectiveness and advantages, further validation is required for the clinical application of this method. In future research, in vitro experiments will be conducted building upon the current simulation calculations, serving as the next step for the clinical application of Proton-CAT.

Reference

- [1] Soerjomataram I, Bray F. Planning for tomorrow: global cancer incidence and the role of prevention 2020–2070. *Nat Rev Clin Oncol* 2021;18:663–72. <https://doi.org/10.1038/s41571-021-00514-z>.
- [2] Mohan R, Grosshans D. Proton therapy – Present and future. *Adv Drug Deliv Rev* 2017;109:26–44. <https://doi.org/10.1016/j.addr.2016.11.006>.
- [3] Mohan R. A review of proton therapy – Current status and future directions. *Precis Radiat Oncol* 2022;6:164–76. <https://doi.org/10.1002/pro6.1149>.
- [4] Tran NH, Shtam T, Marchenko YY, Konevega AL, Lebedev D. Current State and Prospectives for Proton Boron Capture Therapy. *Biomedicines* 2023;11:1727. <https://doi.org/10.3390/biomedicines11061727>.
- [5] Jones B, McMahon SJ, Prise KM. The Radiobiology of Proton Therapy: Challenges and Opportunities Around Relative Biological Effectiveness. *Clin Oncol* 2018;30:285–92. <https://doi.org/10.1016/j.clon.2018.01.010>.
- [6] Lipengolts AA, Finogenova YA, Skribitsky VA, Grigorieva EY. Binary technologies of malignant tumors radiotherapy. *J Phys Conf Ser* 2021;2058:012039. <https://doi.org/10.1088/1742-6596/2058/1/012039>.
- [7] Durante M, Debus J. Heavy Charged Particles: Does Improved Precision and Higher Biological Effectiveness Translate to Better Outcome in Patients? *Semin Radiat Oncol* 2018;28:160–7. <https://doi.org/10.1016/j.semradonc.2017.11.004>.
- [8] Yoon D-K, Jung J-Y, Suh TS. Application of proton boron fusion reaction to radiation therapy: A Monte Carlo simulation study. *Appl Phys Lett* 2014;105:223507. <https://doi.org/10.1063/1.4903345>.
- [9] Matsumoto Y, Fukumitsu N, Ishikawa H, Nakai K, Sakurai H. A Critical Review of Radiation Therapy: From Particle Beam Therapy (Proton, Carbon, and BNCT) to Beyond. *J Pers Med* 2021;11:825. <https://doi.org/10.3390/jpm11080825>.
- [10] Cirrone GAP, Manti L, Margarone D, Petringa G, Giuffrida L, Minopoli A, et al. First experimental proof of Proton Boron Capture Therapy (PBCT) to enhance protontherapy effectiveness. *Sci Rep* 2018;8:1141. <https://doi.org/10.1038/s41598-018-19258-5>.
- [11] Liu D, Lee SL, Wo* J-K. Evaluation of Proton-Boron Fusion-Enhanced Proton Therapy (PBFEP) by Using a Simulation Method. *New Phys Sae Mulli* 2019;69:215–20. <https://doi.org/10.3938/NPSM.69.215>.
- [12] Kim M-S, Wai-Ming Law M, Djeng S-K, Shin H-B, Choi M-G, Kim Y-J, et al. Synergy effect of alpha particles by using natural boron in proton therapy: Computational verification. *AIP Adv* 2019;9:115017. <https://doi.org/10.1063/1.5124322>.
- [13] Meyer HJ, Titt U, Mohan R. Technical note: Monte Carlo study of the mechanism of proton–boron fusion therapy. *Med Phys* 2022;49:579–82. <https://doi.org/10.1002/mp.15381>.
- [14] Mazzone A, Finocchiaro P, Meo SL, Colonna N. On the (un)effectiveness of Proton Boron Capture in Proton Therapy 2018.
- [15] Spraker MC, Ahmed MW, Blackston MA, Brown N, France RH, Henshaw SS, et al. The $^{11}\text{B}(\text{p},\alpha)^8\text{Be} \rightarrow \alpha + \alpha$ and the $^{11}\text{B}(\alpha,\alpha)^{11}\text{B}$ Reactions at Energies Below 5.4 MeV. *J Fusion Energy* 2012;31:357–67. <https://doi.org/10.1007/s10894-011-9473-5>.

- [16] Kokkoris M, Kafkarkou A, Paneta V, Vlastou R, Misaelides P, Lagoyannis A. Differential cross sections for the $^{11}\text{B}(p,\alpha)^8\text{Be}$ and $^{11}\text{B}(p,p^0)^{11}\text{B}$ reactions, suitable for ion beam analysis. *Nucl Instrum Methods Phys Res Sect B Beam Interact Mater At* 2010;268:3539–45. <https://doi.org/10.1016/j.nimb.2010.09.013>.
- [17] Schardt A, Fowler WA, Lauritsen CC. The Disintegration of N^{15} by Protons. *Phys Rev* 1952;86:527–35. <https://doi.org/10.1103/PhysRev.86.527>.
- [18] Tsujii H, Kamada T, Shirai T, Noda K, Tsuji H, Karasawa K, editors. *Carbon-Ion Radiotherapy: Principles, Practices, and Treatment Planning*. Tokyo: Springer Japan; 2014. <https://doi.org/10.1007/978-4-431-54457-9>.
- [19] Kraft G, Kraft-Weyrather W, Ritter S, Scholz M, Stanton J. Cellular and subcellular effect of heavy ions: A comparison of the induction of strand breaks and chromosomal aberration with the incidence of inactivation and mutation. *Adv Space Res* 1989;9:59–72. [https://doi.org/10.1016/0273-1177\(89\)90423-7](https://doi.org/10.1016/0273-1177(89)90423-7).
- [20] Reinfeld BI, Madden MZ, Wolf MM, Chytil A, Bader JE, Patterson AR, et al. Cell-programmed nutrient partitioning in the tumour microenvironment. *Nature* 2021;593:282–8. <https://doi.org/10.1038/s41586-021-03442-1>.
- [21] Barth RF, Zhang Z, Liu T. A realistic appraisal of boron neutron capture therapy as a cancer treatment modality. *Cancer Commun* 2018;38:1–7. <https://doi.org/10.1186/s40880-018-0280-5>.
- [22] Agostinelli S, Allison J, Amako K, Apostolakis J, Araujo H, Arce P, et al. Geant4—a simulation toolkit. *Nucl Instrum Methods Phys Res Sect Accel Spectrometers Detect Assoc Equip* 2003;506:250–303. [https://doi.org/10.1016/S0168-9002\(03\)01368-8](https://doi.org/10.1016/S0168-9002(03)01368-8).
- [23] Zacharatou Jarlskog C, Paganetti H. Physics Settings for Using the Geant4 Toolkit in Proton Therapy. *IEEE Trans Nucl Sci* 2008;55:1018–25. <https://doi.org/10.1109/TNS.2008.922816>.
- [24] Bortfeld T, Schlegel W. An analytical approximation of depth - dose distributions for therapeutic proton beams. *Phys Med Biol* 1996;41:1331–9. <https://doi.org/10.1088/0031-9155/41/8/006>.
- [25] Jette D, Chen W. Creating a spread-out Bragg peak in proton beams. *Phys Med Biol* 2011;56:N131–8. <https://doi.org/10.1088/0031-9155/56/11/N01>.
- [26] Ronsivalle C, Nichelatti E, Picardi L, Montekali RM. Semianalytical tool for spread-out Bragg peak optimization in an active energy-modulation proton therapy linac. *Nucl Instrum Methods Phys Res Sect Accel Spectrometers Detect Assoc Equip* 2021;988:164924. <https://doi.org/10.1016/j.nima.2020.164924>.
- [27] Experiments on the transmutation of elements by protons. *Proc R Soc Lond Ser Contain Pap Math Phys Character* 1933;141:259–81. <https://doi.org/10.1098/rspa.1933.0117>.
- [28] deBoer RJ, Boeltzig A, Macon KT, Aguilar S, Gomez O, Frenz B, et al. Investigation of secondary γ -ray angular distributions using the $\text{N}^{15}(p, \alpha^1\gamma)\text{C}^{*12}$ reaction. *Phys Rev C* 2021;103:065801. <https://doi.org/10.1103/PhysRevC.103.065801>.
- [29] Cho J, Grogg K, Min CH, Zhu X, Paganetti H, Lee HC, et al. Feasibility study of using fall-off gradients of early and late PET scans for proton range verification. *Med Phys* 2017;44:1734–46. <https://doi.org/10.1002/mp.12191>.

